

Thermal chiral anomaly in the magnetic-field induced ideal Weyl phase of $\text{Bi}_{1-x}\text{Sb}_x$ topological insulators

Dung Vu (1), Wenjuan Zhang (2), Cüneyt Şahin (3,4), Michael E. Flatté (3,4), Nandini Trivedi (2), Joseph P. Heremans (1,2,5)

1. Department of Mechanical and Aerospace Engineering, The Ohio State University, Columbus, Ohio 43210

2. Department of Physics, The Ohio State University, Columbus, Ohio 43210

3. Department of Physics and Astronomy, The University of Iowa, Iowa City, Iowa 52242

4. Pritzker School of Molecular Engineering, University of Chicago, Chicago, Illinois 60637

5. Department of Material Science and Engineering, The Ohio State University, Columbus, Ohio 43210

Summary

The chiral anomaly is the predicted break down of chiral symmetry in a Weyl semimetal with monopoles of opposite chirality when an electric field parallel to a magnetic field is applied. It occurs because of charge pumping from a positive chirality to a negative chirality monopole. Experimental observation of this fundamental effect has been plagued by concerns about the pathways of the current. Here, we unambiguously demonstrate the thermal analog of the chiral anomaly in topological insulator bismuth-antimony alloys driven into an ideal Weyl semimetal state by a Zeeman field, with the chemical potential pinned at the Weyl points, and in which the Fermi surface has no trivial pockets. The experimental signature is a large enhancement of the thermal conductivity in an applied magnetic field parallel to the thermal gradient that follows the Wiedemann-Franz law.

Introduction

In 1929, Weyl¹ developed a general theory describing relativistic equations of motion for gravitational forces and electron dynamics. Materials whose electrons are described by this theory are Weyl semimetals (WSMs). Nielsen and Ninomiya² predicted an experimental signature for the existence of WSMs: the chiral anomaly. Its importance extends beyond solid-state physics: it provides a mechanism for charge-parity violation³ and the matter/antimatter imbalance in the universe; in condensed-matter materials, the analogous quasiparticle non-conservation is connected with a change in the vacuum state, thus preserving overall electron number.

Previous experimental determination methods for the chiral anomaly are tainted. First, currently investigated WSMs^{4,5,6} are not ideal; their Fermi surfaces contain features other than Weyl nodes. Second, the signature chiral anomaly feature was a negative longitudinal magnetoresistance (MR)⁷; however, the applied magnetic field distorts current lines, sometimes complicating measurement interpretation.

Ideal WSMs have two distinguishing characteristics. First, the band structure has linearly dispersing bands that intersect at Weyl points (WPs) in a system that breaks time reversal symmetry (TRS) or inversion symmetry (IS). Second, the electrochemical potential μ is at the WP energy ($\mu = 0$) within the experimental energy range. In an ideal WSM, there are no trivial bands at energy μ and no unintentional doping. Thus, μ is pinned to the WPs because those points have the minimum system density of states (DOS); an ideal WSM displays no Shubnikov-de Haas (SdH) oscillations. Then, the Fermi surface consists only of WPs with opposite Berry curvatures, W_R right-handed or W_L left-handed. One pair of WPs in the Brillouin zone (BZ) is

the minimum required by the Nielsen-Ninomiya theorem for a TRS-breaking ideal WSM. If multiple WPs exist, they must be degenerate. Experimentally, in an ideal WSM sample, the carrier-concentration imbalance due to unintentional doping must be smaller than the intrinsic concentration. At finite temperature, a nearly equal density of intrinsic holes and electrons is excited thermally.

The chiral anomaly² in ideal WSMs results from applying parallel electric \mathbf{E} and magnetic fields \mathbf{B} along the direction of the WP separation. \mathbf{B} separates the bands into Landau levels (LL), with a 2D DOS proportional to $1/\ell_B^2$, where $\ell_B \equiv \sqrt{\hbar/eB}$ is the magnetic length. A chirality ($\chi = \pm 1$) consequence is that in the extreme quantum limit (EQL), when only the last LL is populated, electrons have only one Fermi velocity per WP: W_R ($\chi = +1$) has only right-moving electrons of velocity v ; W_L ($\chi = -1$) only left-movers of velocity $-v$. \mathbf{E} shifts the electron momentum on the last LL by $\delta k \propto eE\tau$ (τ^{-1} is the inter-WP scattering rate). This generates right-movers by an amount $\delta n_{+1} \propto \delta k_{+1}/\ell_B^2 \propto E\tau/\ell_B^2$ and annihilates left movers by an amount $\delta n_{-1} \propto -E\tau/\ell_B^2$. This particle generation/annihilation process is the chiral anomaly, giving rise to an additional electric current proportional to v and $\delta n_{+1} - \delta n_{-1}$, which is proportional to $E = |\mathbf{E}|$ and $|\mathbf{B}| = \mu_0 H$, where μ_0 is the vacuum permeability, both applied along the z direction. The anomalous contribution to the electrical conductivity generated by N_w degenerate pairs of WPs is:⁷

$$\sigma_{zz} = N_w \frac{e^2 v \tau}{4\pi \hbar \ell_B^2} = N_w \frac{e^3 v \tau}{4\pi \hbar^2} B_z \quad (1).$$

The scientific community has long considered the resulting negative longitudinal MR the crucial experimental chiral anomaly signature.^{4,5,7 8}

Negative MR was observed in many WSMs, e.g., XPn compounds (X=Nb, Ta; Pn=As, Sb)^{4,5,6} and Dirac semimetals^{8,9,10,11}, but also in materials without Weyl points near μ , e.g., XPn₂ compounds^{12,13,14,15} and elemental semimetal Bi⁸. Broadly observing this effect revealed that the negative MR is unlikely a unique chiral anomaly signature; other, classical effects might be present, as discussed next.^{16,17}

The classical effects that make longitudinal MR measurements ambiguous arise because the Lorentz force distorts the current flow spatial distribution in samples with high-mobility (μ_B) electrons under a magnetic field (i.e., when $\mu_B|\mathbf{B}| > 1$). This causes extrinsic, geometry-dependent MR mechanisms. The first is *current jetting*,^{5,12,17,18,19} arising in 4-contact measurements. With $\mathbf{B} \parallel \mathbf{E}$, the Lorentz force concentrates the current in a cyclotron motion near the sample center. Progressively less current passes near the voltage probes as \mathbf{B} increases, lowering the measured voltage and possibly leading to the erroneous conclusion that the resistivity decreases with \mathbf{B} . The second is an extrinsic *positive geometrical MR* that arises if \mathbf{B} is slightly misaligned vis-à-vis the current flow lines. In the present samples, striations present on the surface of a Czochralski-grown crystal²⁰ can overwhelm the MR measurements, and extreme care needs to be taken with the sample alignment and geometry (see SM). Samples with reduced cross-section and smooth edges minimize both effects. Thermal conductivity $\kappa_{zz}(H_z)$ measurements avoid problems with extrinsic MR because there is no external current flow and the lattice contribution to κ maintains a more \mathbf{B} -independent heat flux than charge flux

distribution in the sample (there is a magnetic-field effect on anharmonic phonon scattering²¹, but it is an order of magnitude smaller than the effects discussed here).

Energy transport in WSMs poses theoretical challenges not encountered in charge transport. From the equations of motion of charge carriers at the WP and the Boltzmann transport equation, we write the imbalance between left and right moving particles (δn_χ) and energy ($\delta \varepsilon_\chi$, the *thermal chiral anomaly*) in the presence of both an electric field \mathbf{E} and thermal gradient $\nabla_r T$ as:²²

$$\delta n_\chi = \frac{\chi e^2 \tau}{4\pi^2 \hbar^2} [\mathbf{B} \cdot \mathbf{E}] C_0 + \frac{\chi e \tau}{4\pi^2 \hbar^2} \left[\mathbf{B} \cdot \frac{-\nabla_r T}{T} \right] C_1 \quad (2)$$

$$\delta \varepsilon_\chi = \frac{\chi e^2 \tau}{4\pi^2 \hbar^2} [\mathbf{B} \cdot \mathbf{E}] (\mu C_0 + C_1) + \frac{\chi e \tau}{4\pi^2 \hbar^2} \left[\mathbf{B} \cdot \frac{-\nabla_r T}{T} \right] (\mu C_1 + C_2) \quad (3)$$

where $C_m = \int (\varepsilon - \mu)^m \left(-\frac{\partial f_0}{\partial \varepsilon} \right) d\varepsilon$, $m \in \{0, 1, 2, \dots\}$ with f_0 the Fermi-Dirac distribution function.

The thermal chiral anomaly thus has two terms: First, a temperature gradient $\nabla_r T$ alone, disregarding any induced electric field, creates an imbalance between the energy carried by the left and right movers while maintaining equal populations when $\mu = 0$ ($C_1 = 0$, $\delta n_\chi = 0$, $\delta \varepsilon_\chi \neq 0$). This response contrasts with the electrical case where $\nabla_r T = 0$ and \mathbf{E} create an imbalance between the populations of left and right movers while, when $\mu = 0$, maintaining the same total energy ($\delta n_\chi \neq 0$, $\delta \varepsilon_\chi = 0$). Second, when the sample is mounted in open-circuit conditions and no external electric field is applied, applying $\nabla_r T$ induces a Seebeck electric field $\mathbf{E} = S (-\nabla_r T)$ (S is the thermopower), driving both $\delta n_\chi \neq 0$ and $\delta \varepsilon_\chi \neq 0$. This creates an additional $\kappa_{zz}(H_z)$ term, the ambipolar thermal conductivity,²³ $S^2 T \sigma$ (see SM). The total thermal conductivity becomes

$\kappa_{zz} = \kappa_{zz,0} + S^2\sigma T$, where $\kappa_{zz,0}$ denotes the energy carried directly by the charge carrier. For completeness, we mention that anomalously large quantum oscillations in the $\kappa_{zz}(H_z)$ of TaAs²⁴ is interpreted as a manifestation of chiral zero sound. We see no evidence for this behavior in Bi_{1-x}Sb_x (x>10%) alloys.

The experimental tests for these theories are first to observe an increase in electronic thermal conductivity in a longitudinal magnetic field, and second to verify the Wiedemann-Franz law (WFL) in the EQL:

$$\kappa_{zz} = LT\sigma_{zz} \quad (4),$$

with L the Lorenz ratio. If each electron carries charge e and entropy k_B , and conserves its energy during scattering, $L = L_0 = \pi^2/3 \left(k_B/e\right)^2$. The experiment consists in testing the ratio $\kappa_{zz}/T\sigma_{zz}$, which we define as L , against the independent variables H_z and T , and, if L is independent of these, to verify if the value equals L_0 . In particular, a Weyl semimetal in which inelastic scattering is limited by the inter-WP scattering time τ , in the quasi-classical limit at $H=0$ is expected to have $L = 7\pi^2/5 \left(k_B/e\right)^2$ but $L=L_0$ in the EQL (see SM and Ref²⁵). In the presence of ambipolar conduction $L>L_0$, because L_0 applies only to $\kappa_{zz,0}$. Extrinsic effects result in underestimations (current jetting) or overestimations (geometrical MR) of L .

In this paper we report the thermal conductivity $\kappa_{zz}(H_z)$ dependence on H_z , and show experimentally that the chiral anomaly affects energy and charge transport similarly, i.e.,

$d\kappa_{zz}/dH_z > 0$, as expected from Eq. (1) and (4). We then experimentally derive values for L .

Previous $\kappa_{zz}(H_z)$ measurements exist: a 1% experimental increase in κ_{zz} for GdPtBi has been reported at $H_z=9$ T.²⁶ However, those samples exhibited SdH oscillations in their MR, which proves that their μ is not at the WPs. An excess κ_{zz} also is observed in NbP,²⁷ dubbed a gravitational anomaly due to the formal link^{28,29} between gradients $\nabla\Phi$ in the gravitational field and $\nabla_r T$. Here, we report $\kappa_{zz}(H_z)$ in magnetic-field induced ideal WSMs, Bi_{1-x}Sb_x alloys with x = 11 and 15 at.%. We demonstrate that these alloy samples, topological insulators (TIs) at $|\mathbf{B}|=0$,³⁰ become WSMs without trivial bands in a quantizing magnetic field along the trigonal axis ($z=[001]$). We further identify the WP locations. In these material samples, we show their carrier concentrations are intrinsic above ~ 30 K, where the relevant κ_{zz} data are collected. This makes them ideal WSMs by construction. Their $\kappa_{zz}(H_z)$ shows an electronic thermal conductivity increase by up to 300% at 9 T. Lorenz ratio $L = \kappa_{zz} / T\sigma_{zz}$ measurements show that $L \approx L_0$. Four experimental observations support relating these thermal conductivity results to the chiral anomaly:

- The effect is robust to disorder, being observed on five samples with two different compositions and mobilities at 10 to 12 K ranging from 1.9×10^6 to 2×10^4 cm²V⁻¹s⁻¹;
- The dependence of κ_{zz} on the direction of \mathbf{B} ;
- The absence of the effect in samples that are similar in composition, but fall outside the range of compositions where WSMs form; and

- The temperature dependence of the observation is insensitive to phonon scattering but shows an activated behavior, with activation energy equal to the bandwidth of the Weyl bands.

Field-induced $\text{Bi}_{1-x}\text{Sb}_x$ Weyl Semimetals.

In this section, we show $\text{Bi}_{1-x}\text{Sb}_x$ alloys ($\sim 9 < x < \approx 18$ at%) become ideal WSMs in a magnetic field H_z above a critical threshold H_C in three steps: We establish (1) their conduction and valence bands cross at H_C , (2) two crossing points appear that are Berry curvature monopoles, i.e., WPs, that increase further in field, and (3) there are no trivial bands.

First, to determine that the conduction and valence bands cross at H_C , we examine the band structure evolution of $\text{Bi}_{1-x}\text{Sb}_x$ alloys as a function of x composition and an applied magnetic field along the [001] direction (**Figure 1**). At zero magnetic field (**Fig. 1(a)-(e)**), the alloys evolve with increasing x through four successive types:³¹ conventional semimetals, semimetals with an inverted band at the BZ L-point, semiconductors, and TIs. Even though the band structure (**Fig. 1(a)**)³¹ is known experimentally, we needed a band-structure calculation to derive the Landé factors, which form a g -tensor (rather than a g -factor) in the Bi-Sb alloy system. The anticipated electronic structure details of the Bi-Sb alloy change slowly as band positions change relative to the chemical potential. The nearly unchanged intrinsic spin-Hall conductivity calculated through the semimetal-TI transitions indicates this.³² A tight-binding Hamiltonian describes the band structure of unalloyed bismuth and antimony,³³ incorporating the s - and p -orbitals of the two atoms in the conventional hexagonal unit cell. The alloy electronic structure is calculated (see SM) using a modified virtual crystal approximation (VCA) in which the tight-binding parameters are obtained directly from those of the elemental semimetals. The calculated

band-edge evolution shown in **Fig. 1(a)** agrees with previous experiments^{34,35,36} within the experimental uncertainty on compositions (1 at.%).

With these parameters, we show that a quantizing magnetic field along the trigonal direction of the TIs (**Fig. 1(f)-(k)**) inverts the bands again. The total Hamiltonian $H = H_{ib} + H_{SOC} + H_{Zeeman}$, with $H_{Zeeman} = -g_{\text{eff}}\mu_B \mathbf{S} \cdot \mathbf{H} \equiv -\mathbf{S} \cdot \mathbf{H}$, describes the Zeeman coupling effect on the alloy electronic structure $H_{ib} + H_{SOC}$, including spin-orbit coupling. The g_{eff} -tensors at the high-symmetry BZ L- and T-points are calculated per Ref. [37] for valence and conduction bands. The T-point g_{eff} -tensor has only one non-zero component, $g_{hz} = 20.5$, which only couples to the magnetic field along z . The more complicated effective g_{eff} -tensor at the L-point shows significant asymmetry. For the conduction and valence bands at the Bi₈₉Sb₁₁ L-point with a magnetic field applied along the trigonal direction, the calculated values are $g_z = -77.5$ and -72.3 , respectively. SdH oscillations³⁸ in Bi confirm the extremely large g -factor values experimentally. This results in an anomalously large effective Zeeman splitting energy $\Delta\varepsilon_z = -\mu_B g_z B_z \approx -4.2$ meV/T at the L-point that overwhelms the orbital splitting of the LLs. Consequently, the band gaps close (**Fig. 1f,h**) at a critical field H_C , calculated to be ~ 3 T for alloy compositions near $x=11\%$. Magnetic-field-induced band closings are uncommon, but have been reported via magneto-optical measurements on Bi³⁹. H_C is sensitive to parameter values used in calculations, and is of the order of 1–4 T. At $H_z > H_C$, the Zeeman energy increase further splits the degeneracy of the Kramers doublets (points W in **Fig. 1(i)**).

For step two, we demonstrate that the Kramers doublets become WPs resulting from explicit TRS breaking by showing that the Chern number changes by an integer for a momentum slice taken between these WPs. The Chern number is an integer that counts the monopoles enclosed in a

given Gaussian surface in the BZ.

We calculate the Berry curvature distribution $\Omega_n(\mathbf{k})$ in momentum space for the alloy band structure to search for the WPs where the Berry curvature is concentrated and singular (see SM). The two WPs carry monopole Berry curvature $\Omega(\mathbf{k}) = \chi \mathbf{k}/k^3$ with opposite chirality, $\chi = \pm 1$. Integrating the Berry curvature provides the Chern number (see SM). A Chern number integer change provides evidence of a topology change and existence of WPs, a pair of points separated symmetrically near each L-point in the 3D BZ (**Fig. 1(j)**). WPs are located by determining the Berry curvature monopole locations and opposite chirality nodes $\chi = \pm 1$ (position provided schematically in **Fig. 1(k)**; precise coordinates given in the SM for an external field $H_z = 8$ T). The separation between the two WPs is in the binary-trigonal plane with a major component along the trigonal direction, which coincides with the external magnetic field direction and a minor component along the bisectrix direction.

Finally, to ascertain that the $\text{Bi}_{89}\text{Sb}_{11}$ system is an ideal WSM at $H_z > H_C$, the model verifies that no trivial bands contribute to transport: neither the T-point band nor any new bands move near μ with increasing H_z . In a semiconductor or semimetal without unintentional doping, μ is pinned at the energy of the lowest DOS, which, without trivial bands, occurs at the WPs. Therefore, if we can minimize unintentional doping experimentally, our experimental systems described below form ideal WSMs by construction.

Experimental

Evidence for the thermal chiral anomaly is shown in six single-crystal samples of $\text{Bi}_{1-x}\text{Sb}_x$, $x \sim 11$ and 15 at%. For control, we report the absence of the anomaly in two semi-metallic samples with $x \approx 5\%$; for this composition an ideal WSM does not exist. The sample compositions

and characterizations are presented in the methods section. The temperature dependence of the resistivity and low-field Hall effect of the best samples (#1 with $x=11\%$ and $x=15\%$) are used to derive carrier concentration and mobility (**Fig. 2 (a-b)**) showing that charge carriers freeze out. This, and the absence of SdH oscillations in the high-field longitudinal magneto-resistivity down to 2 K (SM) and other transport properties (SM), indicate that they are ideal WSMs. The zero-field thermal conductivity κ_{zz} along the trigonal direction of sample #1 is given in **Fig. 2(c)** (for $x=15\%$, SM). It consists of a phonon κ_L and electronic κ_E contribution separated by measuring $\kappa_{zz}(H_y)$ (SM) which shows a steady decrease to a saturation value at high field. This is the ordinary behavior of high-mobility materials^{40,41} used to isolate $\kappa_L = \lim_{H_y \rightarrow \infty}(\kappa_{zz}(H_y))$ for $T < 120$ K. At $T > 120$ K, $\kappa_L(T)$ is extrapolated following a $T^{-1/3}$ law⁴¹ to 300 K. κ_L dominates κ_{zz} below 35 K, limiting measurements of κ_E to $T > 35$ K. At zero field, $\kappa_E(H_z=0)$ follows the WFL with $L=L_0$ (dashed line in **Fig. 2(c)**) above 30 K.

Figure 3 shows the longitudinal magneto-thermal conductivity $\kappa_{zz}(H_z)$ of three samples: **(a)** Bi₉₅Sb₅ (not a WSM); **(b)** Bi₈₉Sb₁₁, and **(c)** Bi₈₅Sb₁₅; (both WSMs above 1–2 T). $\kappa_E(H_z)$ of Bi₈₉Sb₁₁ is reported as a function of H_z in **Fig. 3(d)**: the relative κ_E increase in magnetic field reaches above 300% from 34 to 85 K at 9 T. At low field, $d\kappa_{zz}/dH_z < 0$ for $H_z < 1$ T at $T < 50$ K and $H_z < 3$ T at $T=160$ K. Here, the last LLs of the conduction and valence bands have not crossed in energy. At high field, in WSM phase, $d\kappa_{zz}/dH_z > 0$. We posit the large increase in $\kappa_{zz}(H_z)$ (**Fig. 3(b-d)**) at high field is experimental evidence for the thermal chiral anomaly. The following observations justify the thesis. First, **Fig. 3(a)** shows that $d\kappa_{zz}/dH_z < 0$ at all fields for Bi₉₅Sb₅, which in zero field is a conventional semimetal, not a TI, with a trivial hole pocket in its

Fermi surface at the BZ T-point. In Bi₉₅Sb₅, the band crossing with field does not create an ideal WSM phase; if the $d\kappa_{zz}/dH_z > 0$ observation on Bi₈₉Sb₁₁ and Bi₈₅Sb₁₅ resulted from effects other than the chiral anomaly, e.g., ionized impurity scattering,⁴² known to be weak even in doped Bi,²⁰ it also would occur in similarly prepared Bi₉₅Sb₅. Second, to ascertain that a circulating current or an artifact on the sample surfaces does not induce the effect, samples of Bi₉₅Sb₅ and Bi₈₉Sb₁₁ were mounted with its top and bottom faces covered by electrically conducting Ag epoxy (see SM). We observe no effect from the added surface conducting layers. Third, the $d\kappa_{zz}/dH_z > 0$ data at high H_z were reproduced on Bi₈₉Sb₁₁ samples 2–4 (see SM), which had a mobility of only $2 \times 10^4 \text{ cm}^2\text{V}^{-1}\text{s}^{-1}$ at 12 K, demonstrating the robustness of the observations vis-à-vis defect scattering. Fourth, $d\kappa_{zz}/dH_z > 0$ in Fig. 3(b-d) is observed up to 200 K, twice the Bi Debye temperature, demonstrating the robustness of the effect to phonon scattering. For $T > 200$ K, $d\kappa_{zz}/dH_z < 0$ at all fields due to thermal smearing of the carrier population between the WPs. The last argument will be presented below: the observation has only one energy scale, the Weyl band width.

Simultaneous $\kappa_{zz}(H_z)$ and MR ($\rho_{zz}(H_z)$) measurements were taken on a specially prepared Bi₈₉Sb₁₁ sample (#6, see methods), and are shown **Fig. 4a**. Subtracting κ_L ⁴¹ from $\kappa_{zz}(H_z)$ gives $\kappa_{zz,E}(H_z)$. The WFL is tested by plotting the product $\kappa_{zz,E}(H_z) \cdot \rho_{zz}(H_z)$ normalized to $L_0 T$ in **Fig. 4b** as function of T for $H_z = 5$ and 9 T. The H_z -dependence of the result is within the error bars, and **Fig. 4b** verifies that the WFL holds in an applied field with $L \approx L_0$. Since the material is an ideal WSM and the WSM phase is induced in EQL, the Lorenz ratio is expected to be L_0 . The error

bar increases with decreasing T as κ_L increasingly dominates $\kappa_{zz}(H_z)$ and becomes as large as the signal below 50 K. κ_L masks the electronic contribution completely below 35 K. This knowledge allows fitting the $d\kappa_{zz}/dH_z$ (inset in **Fig. 4c**) experimental temperature dependence at $T > 60$ K. Using equations (1) and (4) with $L=L_0$, $N_w=12$ to derive the thermal chiral conductivity, then taking its field derivative, we obtain:

$$d\kappa_{zz}/dH_z = \frac{\pi e v k_B^2}{\hbar^2} T \tau \quad (5).$$

Using the calculated $v \approx 4.5 \times 10^5$ m/s (see SM), Eq. (5) can be used to derive the inter-WP scattering time $\tau(T)$, shown in **Fig. 4(c)**. Below ~ 60 K, τ of Bi₈₉Sb₁₁ tends asymptotically to 10^{-12} s and is temperature independent at a value one order of magnitude longer than the electron relaxation time in Bi₉₅Sb₅ at 4.2 K. This suggests a high degree of charge-transport protection. In Bi₈₅Sb₁₅ and at $T > 60$ K in Bi₈₉Sb₁₁, τ increases exponentially with T^{-1} , an activated behavior with activation energy of 34 ± 2 meV for Bi₈₉Sb₁₁ and 15 ± 2 meV for Bi₈₅Sb₁₅. These values are expected when charge carriers are thermally excited above the Weyl bandwidth limit τ . The calculated band width (see SM) at 7.5 T is $E_{BW} = 35$ meV for $x = 10.5$ at.% and $E_{BW} = 20$ meV at 7.5 T for $x = 15.1$ at.%, the measured concentrations in the samples. Overall, the **Fig. 4(c)** data suggest that thermal smearing of the carrier population between the WPs is the main mechanism inhibiting the observed increase in $\kappa_{zz}(H_z)$, and that E_{BW} is the only energy scale in the observations.

The angular dependence of the effect, $\kappa_{zz}(H_\theta)$, is acquired on sample #4: **Fig. 4(d)** reports the increase $\Delta\kappa_E = \kappa_{zz}(H = 9T) - \kappa_{zz,MIN}$ ($\kappa_{zz,MIN}$ is the κ_{zz} value at minimal field). The

angular dependence follows a $\cos(\theta)^n$ law with $n > 4$, a much higher exponent than expected from the component of H_θ projected along z .

Altogether, we posit that the $d\kappa_{zz}/dH_z > 0$ observation constitutes robust experimental evidence for the thermal chiral anomaly in an ideal WSM, impervious to current-line distortions and resulting data-interpretation ambiguities that plague MR measurements. The WFL holds at zero field and in field, with $L \approx L_0$. The robustness of the results vis-à-vis defect and phonon scattering and the fact that the only energy scale is the width of the Weyl bands point to the topological origin of the data.

Methods

We studied four samples of nominal composition $\text{Bi}_{89}\text{Sb}_{11}$, labeled 1-4, one $\text{Bi}_{85}\text{Sb}_{15}$ and one $\text{Bi}_{95}\text{Sb}_5$ sample, cut from four separate single crystals. The $\text{Bi}_{85}\text{Sb}_{15}$ (sample #5) and $\text{Bi}_{89}\text{Sb}_{11}$ (samples #1 and #6) are grown in-house by the TMZ technique (see SM); the $\text{Bi}_{95}\text{Sb}_5$ in-house by the Bridgeman method, and $\text{Bi}_{89}\text{Sb}_{11}$ (samples #2-4) grown by Noothoven van Goor using the Czochralski method.²⁰ Table 1 summarizes the sample compositions and purpose. We checked by X-ray diffraction (XRD) (see SM) the compositional uniformity of the TMZ crystal centers. The $\text{Bi}_{89}\text{Sb}_{11}$ crystal composition (providing sample #1) was 10.5 ± 0.5 at.%, and compositional uniformity was interpolated from that of the crystal to better than 0.1% across the sample size. The $\text{Bi}_{85}\text{Sb}_{15}$ crystal composition was 15.1 ± 0.7 at.%, and the measured sample was uniform to better than 0.1% across the sample size. We measured the low-field Hall effect and resistivity (see SM) of separate TMZ crystal pieces, given in **Fig. 2 (a-b)**. The Hall effect polarity switched from n-type to p-type, indicating almost complete charge-carrier freeze-out. Because Bi and Sb are isoelectronic, achieving freeze-out does not require the exquisite stoichiometric control needed for compound semiconductors, but the starting materials required in-house zone refinement because we could not reach carrier concentrations $< 10^{17} \text{ cm}^{-3}$ with 99.999% pure commercial materials. Three cuts (samples #2, #3, #4) of a separate Czochralski crystal piece showed a κ_{zz} increase in field, and had electron densities and mobilities of $8\times 10^{18} \text{ cm}^{-3}$ and $1,050 \text{ cm}^2\text{V}^{-1}\text{s}^{-1}$ at 300 K, which froze out to $1.4\times 10^{16} \text{ cm}^{-3}$ and $2\times 10^4 \text{ cm}^2\text{V}^{-1}\text{s}^{-1}$ at 12 K. Van Goor determined the composition to be 12%; XRD measurements similar to those on the TMZ crystal give 11.3 ± 0.7 at.%.

Thermal conductivity was measured along the [001] crystal direction with the steady state method in the high-vacuum (10^{-6} Torr), radiation-shielded environment of a Quantum Design

Physical Property Measurement System (PPMS) sample chamber. The heat source was a resistive heater (Omega Engineering, Inc., 120 Ω strain gauge) bonded to a Al_2O_3 plate heat spreader. The heat sink, also an Al_2O_3 plate, was glued to the base of the PPMS's AC puck. The heat source and sink were bonded to the cleaved sample top and bottom using GE varnish to ensure these surfaces were short-circuit free. The thermometers were fabricated thermocouples of 25- μm -diameter copper-constantan couples. The thermometers contacted the sample at different positions along the temperature gradient with epoxy. We conducted measurements at discrete temperatures between 10 K and 300 K. The sample assembly was stabilized thermally at each discrete temperature for 30 minutes before measurement. Magneto-thermal conductivity was measured in a sweeping-down magnetic field from 9 T to -9 T in the PPMS, with sweeping rate of 5 mT/s. Controls software was programmed using LabVIEW. Longitudinal MR measurements $\rho_{zz}(H_z)$ were carried out on sample #6, which was designed with a long, thin geometry ($3 \times 0.4 \times 0.6$ mm) with voltage probe wires attached along the spine of the sample⁸ to minimize current jetting. This, and the fact that the magnetic-field alignment was controlled to $\sim 0.1^\circ$, minimizes the geometrical MR effects. Its surface was etched to smooth out the surface damage from cutting.

The thermal conductivity measurement error is dominated by the sample geometry uncertainty, of the order of 10%, and thermocouple calibration. Heat losses were calculated from the measured instrumental heat leaks, which vary with temperature but are of the order of mW/K above 200 K, much smaller than the thermal conductance of the sample. The Cu-Constantan thermocouples were calibrated in field using a thermal-conductivity measurement on a glass sample (see SM). We presumed in data treatment that they have no magnetic-field dependence. Measured, the field dependence up to 7 T was $<2\%$ down to 80 K, $<5\%$ down to 34 K, but as

much as 10% at 16 K, the lowest-reported κ_{zz} temperature. Thus, all data uncertainty reported in **Figures 3 and 4** above 40 K is better than 14%, representing the aggregate of thermocouple calibration uncertainty and heat losses.

For angular-dependent magneto-thermal conductivity measurements, an angle between the temperature gradient and the magnetic field was created with a pre-fabricated, solid copper wedge at a desired angle. The copper wedge was treated as an additional set of thermal and contact resistances in data analysis.

Data Availability

The datasets generated and/or analyzed during the current study are not publicly available, but are available from the corresponding author on reasonable request.

Acknowledgements

This work was supported by CEM, and NSF MRSEC, under grant number. DMR-2011876. The authors acknowledge useful discussions with Dr. Maria A. H. Vozmediano. Renee Ripley edited the text and contributed to the illustrations.

Author contributions

The experiments were designed and carried out by D.V. and J.P.H., the theory by W.Z., C. S., M. E. F., N. T., and J.P.H. All contributed to the integration between theory and experiment and in writing the manuscript.

Additional information

Supplementary information is available in the online version of the paper. Reprints and permissions information is available online at www.nature.com/reprints.

Correspondence and requests for materials should be addressed to J.P.H.

Competing financial interests

The authors declare no competing financial interests.

REFERENCES

-
- ¹ Weyl, H., “Elektron und Gravitation,” *Z. f. Physik* **53**, 330-352 (1929).
- ² Nielsen, H. B. and Ninomiya, M., “The Adler-Bell-Jackiw anomaly and Weyl fermions in a crystal,” *Phys. Lett.* **130B**, 389-396 (1983).
- ³ Christenson, J. H., Cronin, J. W., Fitch, V. L., and Turlay, R., “Evidence for the 2π Decay of the K_2^0 Meson,” *Phys. Rev. Lett.* **13**, 138-140 (1964).
- ⁴ Arnold, F., Shekhar, C., Wu, S.-C., Sun, Y., dos Reis, R. D., Kumar, N., Naumann, M., Ajeesh, M. O., Schmidt, M., Grushin, A. G., Bardarson, J. H., Baenitz, M., Sokolov, D., Borrmann, H., Nicklas, M., Felser, C., Hassinger, E., and Yan, B., “Negative magnetoresistance without well-defined chirality in the Weyl semimetal TaP,” *Nat. Comm.* **7**, 116157 (2016).
- ⁵ Huang, X., Zhao, L., Long, Y., Wang, P., Chen, D., Yang, Z., Liang, H., Xue, M., Weng, H., Fang, Z., Dai, X., and Chen, G., “Observation of the Chiral-Anomaly-Induced Negative Magnetoresistance in 3D Weyl Semimetal TaAs,” *Phys. Rev. X* **5**, 031023 (2015).
- ⁶ Zhang, C.-L., Xu, S.-Y., Belopolski, I., Yuan, Z., Lin, Z., Tong, B., Bian, G., Alidoust, N., Lee, C.-C., Huang, S.-M., Chang, T.-R., Chang, G., Hsu, C.-H., Jeng, H.-T., Neupane, M., Sanchez, D. S., Zheng, H., Wang, J. Lin, H., Zhang, C., Lu, A.-Z., Shen, S.-Q., Neupert, T., Hasan, M., Z., and Jia, S. “Signatures of the Adler-Bell-Jackiw chiral anomaly in a Weyl fermion semimetal,” *Nat. Commun.* **7**, 10735 (2016).
- ⁷ Spivak, N. Z. and Andreev, A. V., “Magnetotransport phenomena related to the chiral anomaly in Weyl semimetals,” *Phys. Rev. B* **93**, 085107 (2016).
- ⁸ Liang, S., Lin, J., Kushwaha, S., Xing, J., Ni, N., Cava, R. J., and Ong, N. P., “Experimental Tests of the Chiral Anomaly Magnetoresistance in the Dirac-Weyl Semimetals Na_3Bi and GdPtBi ,” *Phys. Rev. X* **8**, 031002 (2018).
- ⁹ Li, Q., Kharzeev, D. E., Zhang, C., Huang, Y., Pletikosic, I., Federov, A. V., Zhong, R. D., Schneeloch, J. A., Gu, G. D., and Valla, T., “Chiral magnetic effect in ZrTe_5 ,” *Nat. Phys.* **12**, 3648 (2016).
- ¹⁰ Li, H., He, H. T., Lu, H. Z., Zhang, H. C., Liu, H. C., Ma, R., Fan, Z. Y., Shen, S. Q., and Wang, J. N., “Negative magnetoresistance in Dirac semimetal Cd_3As_2 ,” *Nat. Commun.* **7**, 10301 (2016).
- ¹¹ Guo, S. T., Sankar, R., Chien, Y. Y., Chang, T. R., Jeng, H. T., Guo, G. Y., Chou, F. C., and Lee, W. L., “Large transverse Hall-like signal in topological Dirac semimetal Cd_3As_2 ,” *Sci. Rep.* **6**, 27487 (2016).

-
- ¹² Li, Y., Li, L., Wang, J. L., Wang, T. T., Xu, X. F., Xi, C. Y., Cao, C., and Dai, J. H., “Field-induced resistivity plateau and unsaturated negative magnetoresistance in topological semimetal TaSb₂,” *Phys. Rev. B* **94**, 121115(R) (2016).
- ¹³ Li, Y. P., Wang, Z., Lu, Y. H., Yang, X. J., Shen, Z. X., Sheng, F., Feng, C. M., Zheng, Y., and Xu, Z., “A Negative Magnetoresistance in Topological Semimetals of Transition-Metal Dipnictides with Nontrivial Z₂ Indices,” arXiv:1603.04056 (2016).
- ¹⁴ Luo, Y. K., McDonald, R. D., Rosa, P. F. S., Scott, B., Wakeham, N., Ghimire, N. J., Bauer, E. D., Thompson, J. D., and Ronning, F., “Anomalous electronic structure and magnetoresistance in TaAs₂,” *Sci. Rep.* **6**, 27294 (2016).
- ¹⁵ Shen, B., Deng, X. Y., Kotliar, G., and Ni, N., “Fermi surface topology and negative longitudinal magnetoresistance observed in the semimetal NbAs₂,” *Phys. Rev. B* **93**, 195119 (2016)
- ¹⁶ ¹⁹ Chambers, R. G. “The conductivity of thin wires in a magnetic field”, *Proc. Roy. Soc.* **A202** 378-394 (1950).
- ¹⁷ Hu, J. S., Rosenbaum, T. F., and Betts, J. B., “Current jets, disorder, and linear magnetoresistance in the silver chalcogenides,” *Phys. Rev. Lett.* **95**, 186603 (2005).
- ¹⁸ Li, Y., Wang, Z., Li, P., Yang, X., Shen, Z., Sheng, F., Li, X., Lu, Y., Zheng, Y., and Xu, Z.-A., “Negative magnetoresistance in Weyl semimetals NbAs and NbP: intrinsic chiral anomaly and extrinsic effects,” *Front. Phys.* **12(3)**, 127205 (2017).
- ¹⁹ dos Reis, R. D., Ajeesh, M. O., Kumar, N., Arnold, F., Shekhar, C., Naumann, M., Schmidt, M., Nicklas, M., and Hassinger, E., “On the search for the chiral anomaly in Weyl semimetals: the negative longitudinal magnetoresistance,” *New J. Phys.* **18**, 085006 (2016).
- ²⁰ Noothoven van Goor, J. M., “Donors and acceptors in bismuth,” Philips Research Report Suppl. 4 (1971).
- ²¹ Jin, H., Restrepo, O. D., Antolin, N., Boona, S. R., Windl, W., Myers, R. C., and Heremans, J. P., “The Phonon-induced Diamagnetic Force and its Effect on the Lattice Thermal Conductivity,” *Nature Materials* **14**, 601-606 (2015).
- ²² Das, K. and Agarwal, A., “Thermal and gravitational chiral anomaly induced magneto-transport in Weyl semimetals”, *Phys. Rev. Research* **2**, 013088 (2020)
- ²³ Gallo, C. F., Chandrasekhar, B. S. and Sutter, P. H. “Transport Properties of Bismuth Single Crystals” *J. Appl. Phys.* **34**, 144 (1963)
- ²⁴ Junsen Xiang, Sile Hu, Zhida Song, Meng Lv, Jiahao Zhang, Lingxiao Zhao, Wei Li, Ziyu Chen, Shuai Zhang, Jian-Tao Wang, Yi-feng Yang, Xi Dai, Frank Steglich, Genfu Chen, and Peijie Sun, “Giant Magnetic Quantum Oscillations in the Thermal Conductivity of TaAs: Indications of Chiral Zero Sound”, *Phys. Rev. X* **9**, 031036 (2019).

-
- ²⁵ Andreev A. V and Spivak B.Z., “Longitudinal Negative Magnetoresistance and Magnetotransport Phenomena on Conventional and Topological Conductors”, *Phys. Rev. Lett.* **120** 026601 (2018)
- ²⁶ Schindler, C., Guin, S. N., Schnelle, W., Kumar, N., Fu, C., Borrmann, H., Shekhar, C., Zhang, Y., Sun, Y., Felser, C., Meng, T., Grushin, A. G., Gooth, J., “Observation of an anomalous heat current in a Weyl fermion semimetal,” arXiv 1810.02300v1 (2018).
- ²⁷ JohannesGooth et al., “Experimental signatures of the mixed axial-gravitational anomaly in the Weyl semimetal NbP”, arXiv 1703.10682
- ²⁸ R. C. Tolman and P. Ehrenfest, “Temperature equilibrium in a static gravitational field”, *Phys. Rev.* **36** 1791-1798 (1930)
- ²⁹ J. M. Luttinger, “Theory of Thermal Transport Coefficients”, *Phys. Rev.* **135** A1505-A1514 (1964)
- ³⁰ Hsieh, D., Qian, D., Wray, L., Xia, Y., Hor, Y. S., Cava, R. J., and Hasan, M. Z., “A topological Dirac insulator in a quantum spin Hall phase,” *Nature* **452**, 970 (2008).
- ³¹ Vandaele, K., Otsuka, M., Hasegawa, Y., and Heremans, J. P., “Confinement Effects, Surface Effects, and Transport in Bi and Bi_{1-x}Sb_x Semiconducting and Semimetallic Nanowires,” *J. Phys.: Condens. Matter* **30**, 403001 (2018).
- ³² Şahin, C. and Flatté, M. E., “Tunable Giant Spin Hall Conductivities in a Strong Spin-Orbit Semimetal: Bi_{1-x}Sb_x,” *Phys. Rev. Lett.* **114**, 107201 (2015).
- ³³ Liu, Y. and Allen, R. E., “Electronic Structure of the semimetals Bi and Sb,” *Phys. Rev. B* **52**, 1566 (1995).
- ³⁴ Cucka, P. and Barrett, C. S., “The Crystal Structure of Bi and of Solid Solutions of Pb, Sn, Sb and Te in Bi,” *Acta Cryst.* **15**, 865 (1962).
- ³⁵ Mendez, E. E., Misu, A., and Dresselhaus, M. S., “Pressure-dependent magnetoreflexion studies of Bi and Bi_{1-x}Sb_x alloys,” *Phys. Rev. B* **24**, 639 (1981).
- ³⁶ Brandt, N. B., Svistova, E. A., and Semenov, M. V., “Electron transitions in antimony-rich bismuth-antimony alloys in strong magnetic fields,” *Sov. Phys. JETP* **32**, 238 (1971).
- ³⁷ Cohen, M. H. and Blount, E. I., “The g-factor and de Haas-van Alphen effect of electrons in bismuth,” *Philos. Mag.* **5**, 50, 115-126 (1960).
- ³⁸ G. E. Smith, G. A. Baraff, and J. M. Rowell, “Effective g-Factor of Electrons and Holes in Bismuth”, *Phys. Rev.* **135**, A1118 (1964).

³⁹ M. P. Vecchi, J. R. Pereira, and M. S. Dresselhaus, “Anomalies in the magnetoreflexion spectrum of bismuth in the low-quantum-number limit”, *Phys. Rev. B* **14**, 298 (1976).

⁴⁰ Heremans, J. P., Shayegan, M., Dresselhaus, M. S., and Issi, J-P., “High Magnetic Field Thermal Conductivity Measurements in Graphite Intercalation Compounds,” *Phys. Rev. B* **26**, 3338-46 (1982).

⁴¹ Kagan, V. D. and Red'ko, N. A., “Phonon thermal conductivity of bismuth alloys,” *Sov. Phys. JETP* **73** (4), 664-671 (1991); translation of *Zh. Eksp. Teor. Fiz.* **100**, 1205-1218 (1991).

⁴² P. N. Argyres and E. N. Adams, “Longitudinal Magnetoresistance in the Quantum Limit”, *Phys. Rev.* **104**, 900-908 (1956).

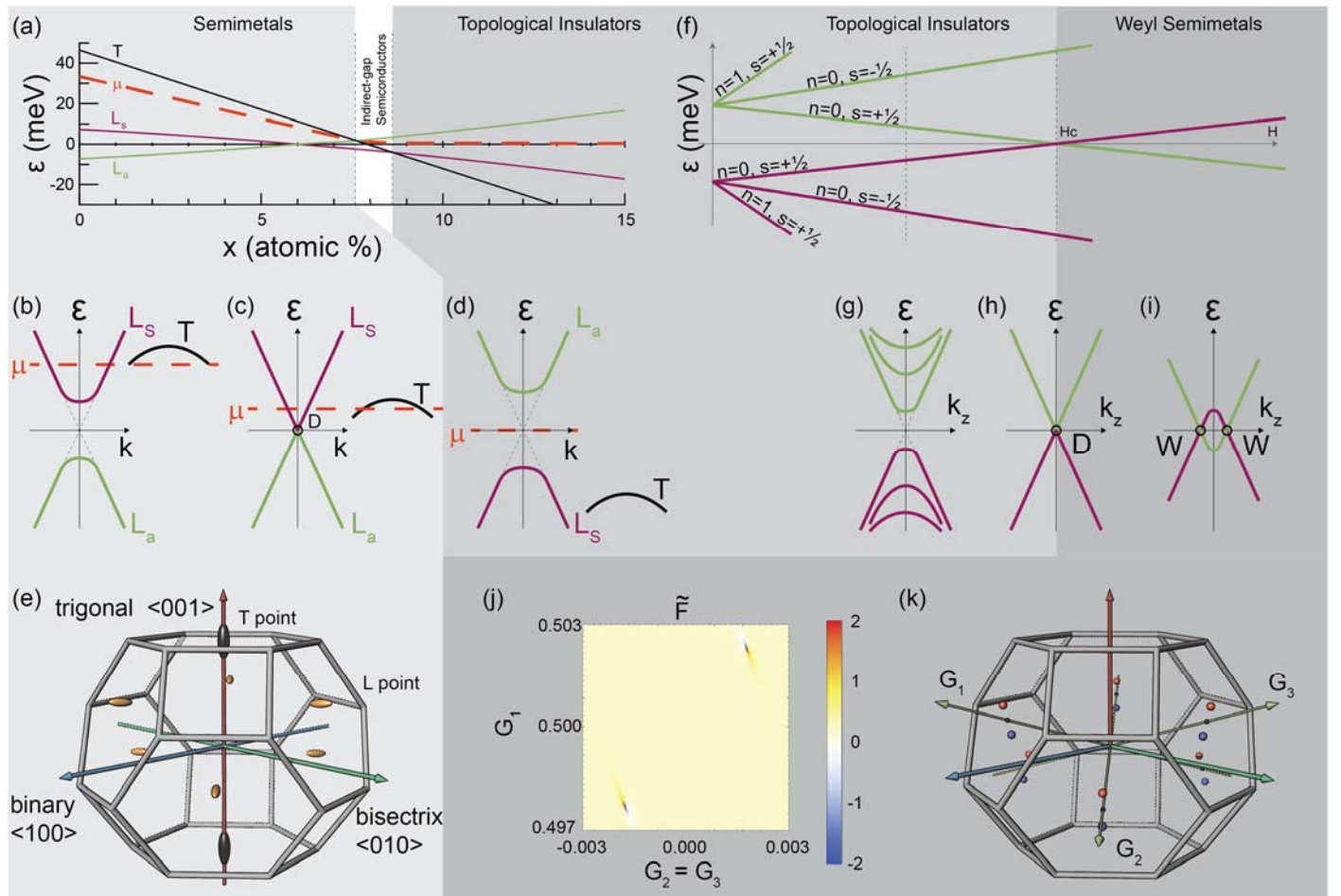


Figure 1 Evolution of $\text{Bi}_{1-x}\text{Sb}_x$ alloys with composition and magnetic field. (a) Band-edge energies' composition dependence at zero applied magnetic field. Elemental semimetal Bi has electrons residing in a conduction band, L_s , and holes in the valence band, T ; with a filled second valence band, L_a . Adding Sb (x in at.%), the $L_a - L_s$ gap closes until the bands intersect near $x \approx 6\%$. The T -band edge intersects that of the L_a and L_s bands at $x \approx 7.7\%$ and $x \approx 8.6\%$, respectively (from VCA, see text). The chemical potential $\mu(x)$ evolution for samples with no unintentional doping is shown as a dashed orange line. Alloys with $x < 7.7\%$ are semimetals with μ in a band; alloys with $x > 8.6\%$ are direct-gap topological insulators (TIs)³¹ with μ at mid-gap in undoped material. (b) Semimetal Bi dispersion relation, (c) $\text{Bi}_{94}\text{Sb}_6$ alloys' Dirac dispersion, and (d) Bi-Sb TIs' dispersion. (e) Bi BZ and Fermi surfaces: electrons fill 6 pockets at the BZ L -points; holes fill 2 pockets at the T -points. (f) TI alloy $\text{Bi}_{89}\text{Sb}_{11}$ band-edge energies in a magnetic field H_z applied along the trigonal direction. The field separates the L_a and L_s valence bands into Landau levels, with orbital quantum number n and spin s . With increasing H_z the $n=0, s=1/2$ of the L_a and L_s bands cross again at a critical field H_C . At higher fields, the crossing points develop into Weyl points (see text). (g) Dispersions along k_z at $H_z < H_C$. (h) Dispersion in k_z at $H_z = H_C$. (i) Dispersion at $H_z > H_C$ becomes that of a field-induced Weyl semimetal. (j) Calculated Berry curvature distribution in the \mathbf{G} axes system, identified in (k). Color contrast highlights the WPs in (j); their location in the BZ is given schematically in (k), ; blue and red points indicate WPs with opposite Berry curvature.

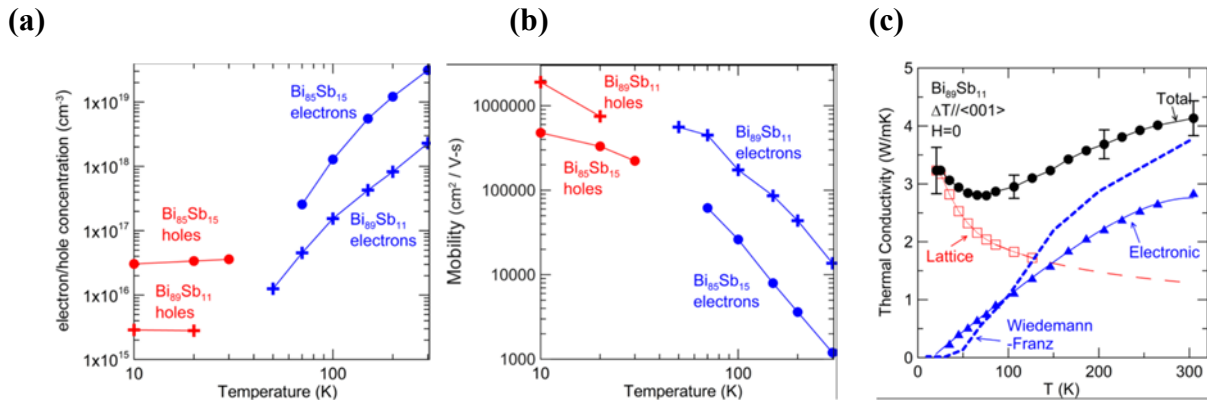


Figure 2: Bi₈₉Sb₁₁ and Bi₈₅Sb₁₅ electronic and thermal properties . (a) carrier concentration and (b) mobility; the samples switch from dominantly n-type at 300 K to dominantly p-type at 10 K. (c) Bi₈₉Sb₁₁ zero-field κ_{zz} separated into lattice κ_L and electronic κ_E parts (see supplement for Bi₈₅Sb₁₅ data). The dashed blue line is κ_E calculated from the resistivity and the Wiedemann-Franz law (WFL) with $L=L_0$.

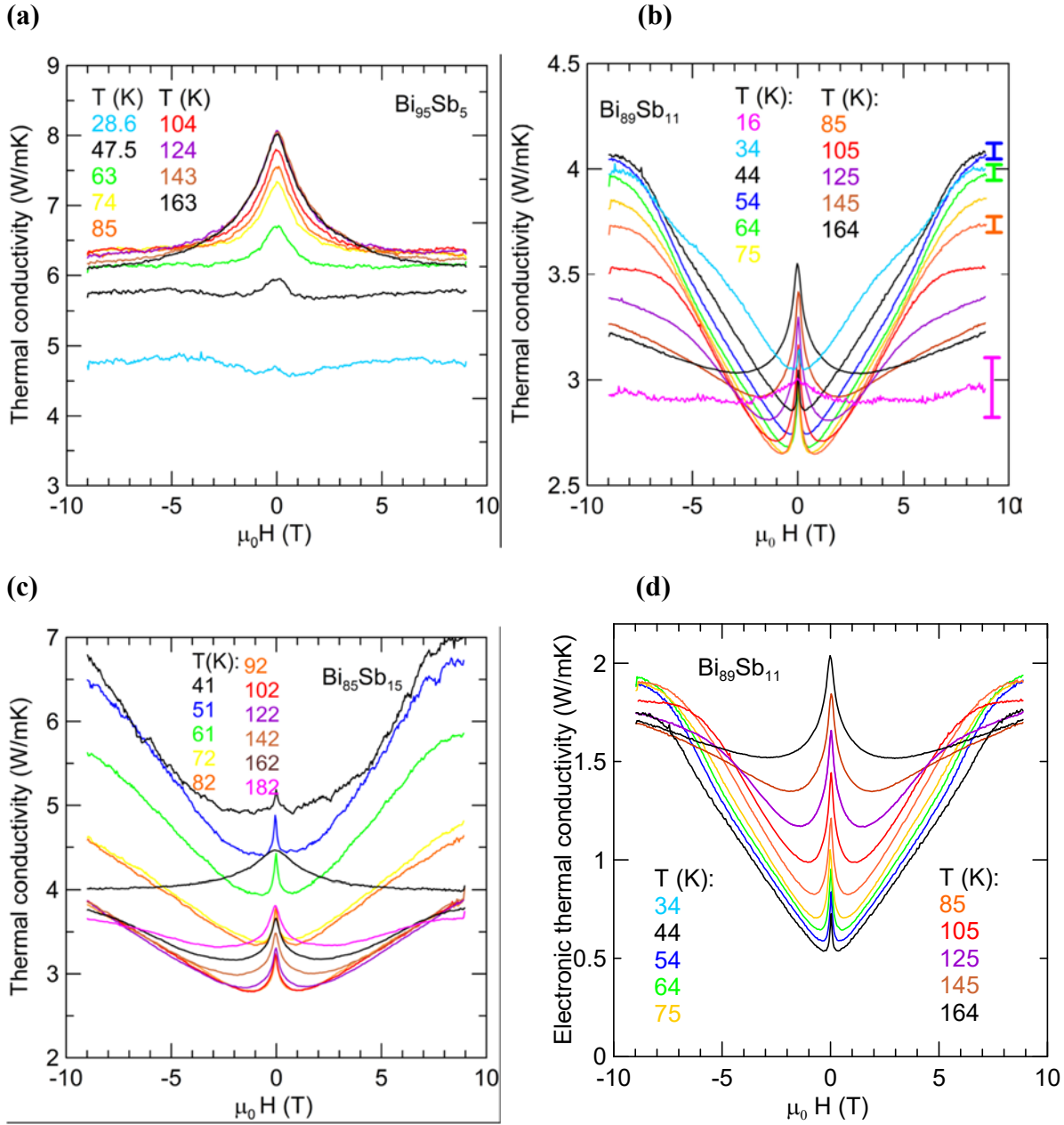


Figure 3: $\text{Bi}_{95}\text{Sb}_5$, $\text{Bi}_{89}\text{Sb}_{11}$, and $\text{Bi}_{85}\text{Sb}_{15}$ thermal conductivity $\kappa_{zz}(H_z)$ dependence on longitudinal magnetic field along the trigonal ($z=\langle 001 \rangle$) direction at temperatures indicated. (a) $\text{Bi}_{95}\text{Sb}_5$, a conventional, not Weyl, semimetal, has $\kappa_{zz}(H_z)$ that monotonically decreases with H_z , due to a positive MR. The $\kappa_{zz}(H_z)$ of (b) $\text{Bi}_{89}\text{Sb}_{11}$ (sample 1) and (c) $\text{Bi}_{85}\text{Sb}_{15}$ shows a decrease due to a conventional positive MR in the TI regime, followed by an increase that we posit is evidence for the thermal chiral anomaly. The error bars (derivation in SM) are relative to the field dependence, not the absolute value. (d) The electronic contribution κ_E of the total thermal conductivity κ_{zz} for $\text{Bi}_{89}\text{Sb}_{11}$ is obtained by subtracting the lattice contribution κ_L . κ_E shows a $>300\%$ increase with field at 9 T. The uncertainty in measurements is described in the methods section.

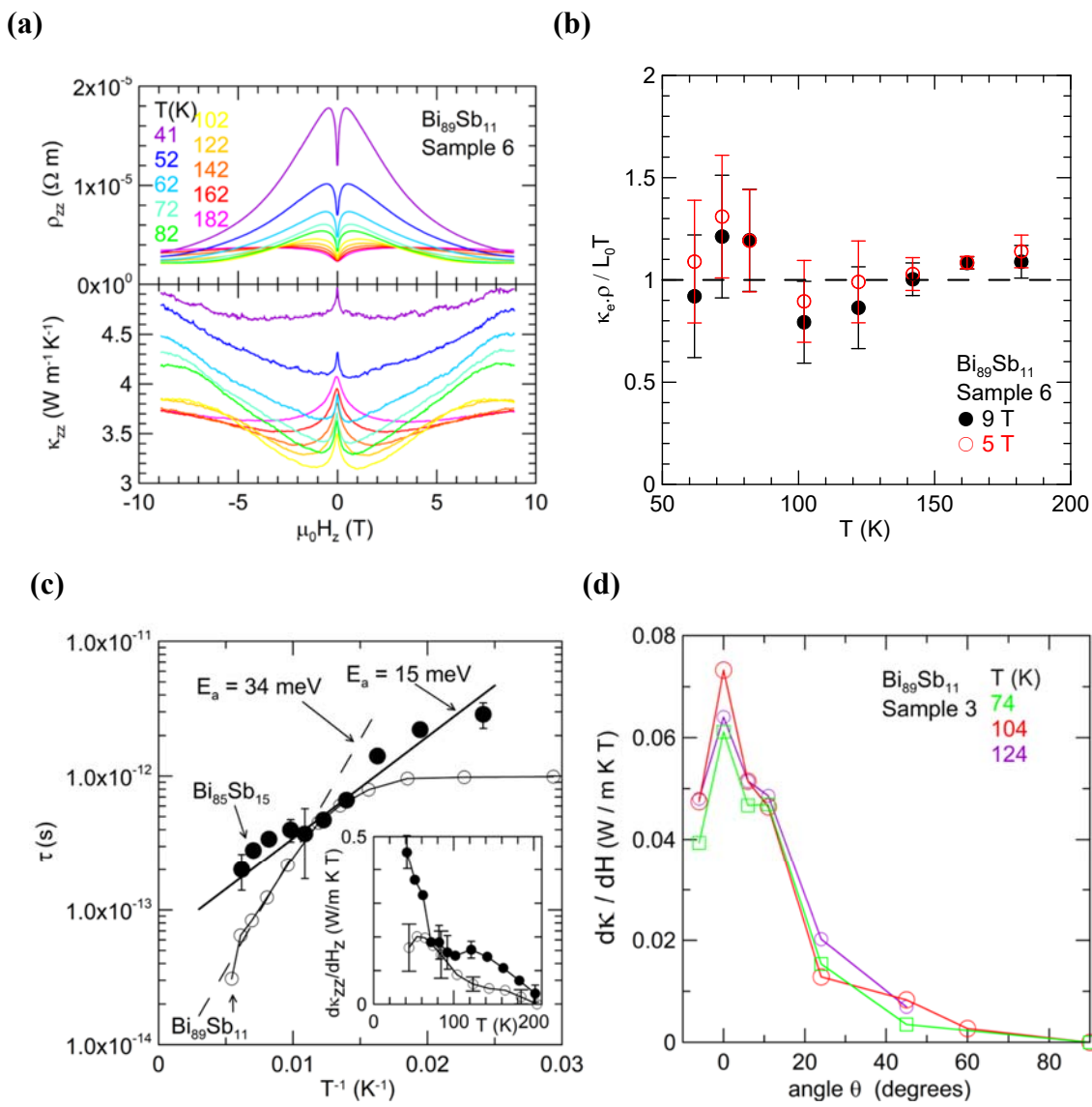


Figure 4 Wiedemann-Franz law verification; temperature and angular dependence of the $\kappa_{zz}(H_z)$ increase. (a) $\text{Bi}_{89}\text{Sb}_{11}$ (sample 6) $\kappa_{zz}(H_z)$ and $\sigma_{zz}(H_z)$ (b) Lorenz ratio $L = \kappa_{zz,e}(H_z) / \sigma_{zz}(H_z)$ derived from (a), normalized to $L_0 T$ at two values of H_z ; L is independent of H_z within the error bar; (c) The inter-WP scattering time τ , derived from equation (5) fits Arrhenius plots (lines) at $T > 60$ K with an activation energy of 34 meV for $\text{Bi}_{89}\text{Sb}_{11}$ and 15 meV for $\text{Bi}_{85}\text{Sb}_{15}$. The inset shows the temperature dependence of $d\kappa_{zz}(H_z)/dH_z$ between 4 and 8 T of TMZ sample #1 $\text{Bi}_{89}\text{Sb}_{11}$ and $\text{Bi}_{85}\text{Sb}_{15}$. (d) $\Delta\kappa_{zz}$ dependence on angle θ defined as $\theta = 0^\circ$ for $H_\theta = H_z$ along [001], and $\theta = 90^\circ$ for $H_\theta = H_y$ along [010].

Sample name	Growth	x	Used for	density	mobility
		at%		cm^{-3}	$\text{cm}^2 \text{V}^{-1} \text{s}^{-1}$
Sample #1	TMZ	10.5±0.5	$\kappa_{zz}(H_z), \kappa_{zz}(H_y)$ $\kappa_{zz}(H_z)$ Ag contacts		
Hall	TMZ	10.5±0.5	Hall, resistivity	3×10^{15} (10 K)	1.9×10^6 (10 K)
Sample #2	Czochralski	11.3±0.7	Negative MR		
		11.3±0.7	Magneto-Seebeck		
		11.3±0.7	$\kappa_{zz}(H_z), \kappa_{zz}(H_y)$		
Sample #3	Czochralski	11.3±0.7	$\kappa_{zz}(H_z), \kappa_{zz}(H_y)$		
		11.3±0.7	$\kappa_{zz}(H_z)$ -angular dependence		
Sample #4	Czochralski	11.3±0.7	$\kappa_{zz}(H_z), \kappa_{zz}(H_y)$		
Hall	Czochralski	11.3±0.7	Hall, resistivity	1.4×10^{16} (12 K)	2×10^4 (12 K)
Sample #5	TMZ	15.1±0.7	$\kappa_{zz}(H_z), \kappa_{zz}(H_y)$		
Hall	TMZ	15.1±0.7	Hall, resistivity	3×10^{16} (10 K)	4.5×10^5 (10 K)
Sample #6	TMZ	10.5±0.5	$\kappa_{zz}(H_z), \rho_{zz}(H_y)$	as #1	as #1
semimetal	Bridgeman	5±0.5	$\kappa_{zz}(H_z)$ $\kappa_{zz}(H_z)$ Ag contacts, Hall, resistivity	4.5×10^{16} (79 K)	8×10^4 (79 K)

Table 1 Samples used in this study.